PAPER

Electronic and relativistic contributions to ion-pairing in polyoxometalate model systems†

Dylan J. Sures,[a] Stefano A. Serapian,[b] Károly Kozma,[a] Pedro I. Molina,[a] Carles Bo[b] and May Nyman*[a]

Ion pairs and solubility related to ion-pairing in water influence many processes in nature and in synthesis including efficient drug delivery, contaminant transport in the environment, and self-assembly of materials in water. Ion pairs are difficult to observe spectroscopically because they generally do not persist unless extreme solution conditions are applied. Here we demonstrate two advanced techniques coupled with computational studies that quantify the persistence of ion pairs in simple solutions and offer explanations for observed solubility trends. The system of study, $([(CH_3)_4N]^+,Cs)_8[M_6O_{19}]$ (M = Nb,Ta), is a set of unique polyoxometalate salts whose water solubility increases with increasing ion-pairing, contrary to most ionic salts. The techniques employed to characterize Cs^+ association with $[M_6O_{19}]^{8-}$ and related clusters in simple aqueous media are ^{133}Cs NMR (nuclear magnetic resonance) quadrupolar relaxation rate and PDF (pair distribution function) from X-ray scattering. The NMR measurements consistently showed more extensive ion-pairing of Cs^+ with the Ta-analogue than the Nb-analogue, although the electrostatics of the ions should be identical. Computational studies also ascertained more persistent $Cs^+-[Ta_6O_{19}]$ ion pairs than $Cs^+-[Nb_6O_{19}]$ ion pairs, and bond energy decomposition analyses determined relativistic effects to be the differentiating factor between the two. These distinctions are likely responsible for many of the unexplained differences between aqueous Nb and Ta chemistry, while they are so similar in the solid state. The X-ray scattering studies show atomic level detail of this ion association that has not been prior observed, enabling confidence in our structures for calculations of Cs-cluster association energies. Moreover, detailed NMR studies allow quantification of the number of Cs^+ associated with a single $[Nb_6O_{19}]^{8-}$ or $[Ta_6O_{19}]^{8-}$ anion which agrees with the PDF analyses.

1 Introduction

Preceding precipitation of ionic salts from water, soluble ion pairs and aggregates must form. When these increase in size and decrease in charge, they precipitate. Elucidating these processes is foundational to designing effective pharmaceuticals,[1] remediating contamination in the environment,[2] optimizing materials synthesis in water,[3] and growing biological and inorganic crystals from water.[4] Aqueous solubility and ion-pairing is extremely complex because many phenomena are involved including the lattice energy of the crystallized or precipitated solid, the hydration sphere of both the cation and anion, the sum of ions present in solution, and pH effects if the cation and/or anion is a polyatomic oxo-ion.[5–7] Alkali salts of polyoxometalates (POMs), the early d^0 Group V/VI metal–oxo clusters, are ideal for probing both ion association[8–12] and crystal

growth mechanisms,[13–18] and these two phenomena are intimately related. POMs scatter X-rays strongly due to their large size and to the high electronic density of the metals present in their structures. This has allowed observation of ion pair formation *via* small-angle X-ray scattering by determining the size of the scattering species.[6] In addition, POMs are molecular metal oxides,[19] so ion-pairing behavior at bulk metal oxide interfaces can be inferred from their study. We do not entirely understand what drives solubility trends of alkali salts. If we simply consider hydration spheres, Li^+ carries a large hydration sphere and does not exhibit extensive ion-pairing, suggesting all Li-salts should be highly soluble in water.[20,21] Yet, some POMs are highly soluble as Li-salts and extremely insoluble as Cs-salts (normal solubility), while others exhibit exactly the opposite solubility trend (anomalous solubility).[8,10,22–24] For instance, the Cs-salt of the hexaniobate POM ($[Nb_6O_{19}]^{8-}$, Fig. 1) is soluble up to 1.5 M, whereas the lithium and sodium salts are only sparingly soluble. We can state, as an initial approximation, that POMs of high charge density exhibit anomalous solubility while POMs of low charge density exhibit normal solubility. Alkali salts of highly charged oxoanions including CO_3^{2-} and PO_4^{3-} also exhibit anomalous solubility.[17,25] Ultimately, we endeavor to explain the anomalous solubility trend

[a] *Department of Chemistry, Oregon State University, 107 Gilbert Hall, Corvallis, OR, 97331-4003, USA. E-mail: may.nyman@oregonstate.edu; Web: http://nyman.chem.oregonstate.edu/*

[b] *Institut Català d'Investigació Química (ICIQ), The Barcelona Institute of Science and Technology, Av. Països Catalans, 17. 43007 Tarragona, Spain*

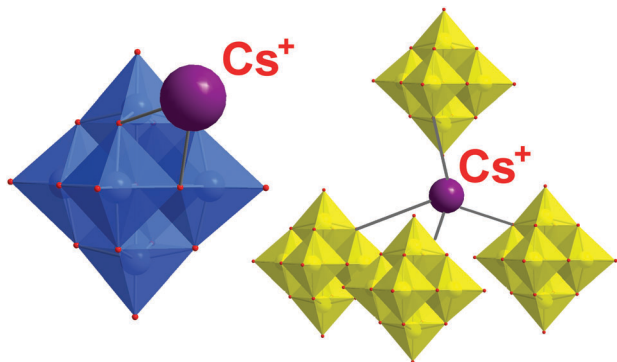† Electronic supplementary information (ESI) available. See DOI: 10.1039/c6cp08454k

Fig. 1 Possible solution-state coordination environments of Cs$^+$ with $[M_6O_{19}]^{8-}$ (M = Nb, Ta; left) and $[Nb_2W_4O_{19}]^{4-}$ (right) from the solid state structures.[27]

in terms of the structuring of ions in solution and also determine exactly the charge density at which the trend reverses. An initial approach was to benchmark solutions in which ion association is forced by employing extreme conditions, including an excess of one of the ions to drive maximum ion association.[9,26] However, these studies are not broadly representative of conditions in natural settings that are of low ionic strength and a complex mixture of ions, nor materials synthesis conditions in which metastable species could persist and be isolated.

Understanding Cs$^+$'s ion association behavior in water is particularly important, as scientists and engineers are currently optimizing efficient technologies to remove radioactive ^{137}Cs from the various contaminated groundwater, seawater, and agricultural environments that are still emerging in the wake of the Fukushima–Daiichi nuclear disaster.[28–30] Solubility and ion-pairing was used to separate ppm levels of Cs from nuclear wastes containing ∼3 moles of Na–sodium tetraphenylborate is soluble while Cs tetraphenylborate is insoluble.[31] Of additional importance, Cs$_8$[Nb$_6$O$_{19}$] was used as a model system to computationally probe the base hydrolysis reactivity of $[Nb_6O_{19}]^{8-}$, where the Cs-association is expected to simplify hydrolysis effects in both solution and solid state reactions.[32]

Despite the similarities between hexaniobate ({Nb$_6$}) and hexatantalate ({Ta$_6$}) in the solid state, we and others have noted considerable differences in solution behavior,[33–36] but the fundamental origin of these differences has never been explained, other than by inference to broadly defined effects of frontier f-orbitals present in {Ta$_6$} but not {Nb$_6$}. Next to Zr and Hf, Nb and Ta are the two elements on the periodic table that are the most chemically similar as a direct consequence of the lanthanide effect. This report provides insight into how the lanthanide effect alters the solution behavior of post-lanthanide metals compared to their lighter counterparts. Here we utilize two advanced spectroscopies that permit probing solutions of relatively low ionicity and yield unprecedented details concerning solution phase ion association. POMs of this study provide a range of charge density while the structure remains similar or identical. These include Cs-salts of: $[M_6O_{19}]^{8-}$, $[Nb_4W_2O_{19}]^{6-}$, $[Nb_2W_4O_{19}]^{4-}$ and $[MW_9O_{32}]^{5-}$ (M = Nb, Ta).[27,37,38] The quadrupolar relaxation rate of ^{133}Cs by Nuclear Magnetic Resonance

(NMR) and X-ray total scattering, explained by computational models point towards the influence of relativistic effects in the formation of ion pairs and as a source of differences between Nb(v) and Ta(v) speciation in water. X-ray scattering revealed the structure of the Cs-POM association in solution. Furthermore, with detailed analysis of the NMR data, we quantified the average number of Cs$^+$ associated with clusters in solution, which agrees with the model proposed by the X-ray scattering data. Taken together, these data support a proposed model for discrete ion pairs (meaning not bridged into large networks) paired with anomalously high solubility.

2 Experimental

2.1 Syntheses

Cs-salts of POMs (Cs$_8$[Nb$_6$O$_{19}$]·14H$_2$O, Cs$_8$[Ta$_6$O$_{19}$]·14H$_2$O, Cs$_5$[NbW$_9$O$_{32}$]·7H$_2$O, Cs$_5$[TaW$_9$O$_{32}$]·6.5H$_2$O, Cs$_4$[Nb$_2$W$_4$O$_{19}$]·4H$_2$O, Cs$_4$Na$_2$[Nb$_4$W$_2$O$_{19}$]·10H$_2$O, [(CH$_3$)$_4$N]$_5$[H$_3$Nb$_6$O$_{19}$]·20H$_2$O (TMA{Nb$_6$}), and [(CH$_3$)$_4$N]$_6$[H$_2$Ta$_6$O$_{19}$]·21H$_2$O, (TMA{Ta$_6$})) were synthesized by following the reported procedures.[23,27,38–40] These procedures are also described in detail in the ESI.†

2.2 Inversion-recovery ^{133}Cs NMR

The ^{133}Cs spectra were recorded on a Bruker 400 MHz NMR spectrometer operating at the ^{133}Cs Larmor frequency (52.482 MHz) at a constant temperature of 25 °C (by means of a VTU temperature controller) in solutions of 90% H$_2$O and 10% D$_2$O. T_1 values were derived by inversion recovery experiments (see ESI†). Each value of T_1 was calculated by an exponential fit from 16 delay times of four scans each.

T_1 inversion recovery was performed on 5 mM solutions that were prepared from each of the aforementioned Cs$^+$ POM salts, as well as a range of solution concentrations (0.5 mM to 100 mM) of Cs$_8$Nb$_6$O$_{19}$ and Cs$_8$Ta$_6$O$_{19}$.

Solutions of 20 mM (TMA)$_5$H$_3$[Nb$_6$O$_{19}$] and (TMA)$_6$H$_2$[Ta$_6$O$_{19}$] (TMA = (CH$_3$)$_4$N$^+$) in 200 mM TMAOH were also prepared to assure deprotonation of the clusters. A second series of such solutions, i.e. 20 mM of either hexacoltantate ($[M_6O_{19}]^{8-}$, M = Nb, Ta)[38] in 200 mM TMAOH, was replicated, this time with the addition of 240 mM CsCl. Thus, systematic mixing of these solutions afforded a range of Cs$^+$ concentrations from 10 mM to 240 mM, with a constant hexacoltantate anion concentration of 20 mM.

2.3 CTAB precipitation and atomic ratio analysis

Solutions of 5 mM, 10 mM, and 20 mM Cs$_8$M$_6$O$_{19}$ (M = Nb, Ta) were combined with excess solid cetyltrimethylammonium bromide (CTAB, C$_{16}$H$_{31}$(CH$_3$)$_3$NBr) and a white precipitate was immediately observed. The white precipitate was separated by centrifugation and the resultant solid was dried under vacuum. The surface layer of the solid was scraped off and discarded in order to remove any excess surface Cs$^+$ and atomic ratio analysis was performed on the bulk region of each white powder to determine the approximate ratio of bound Cs$^+$ per hexametalate unit (upon averaging five or more data points per sample) by EDX. EDX Spectra were obtained from a Quanta 600F instrument (FEI).

2.4 Viscometry

Viscosity measurements were taken with an Ostwald Viscosity Tube and a stopwatch at a constant temperature of 25 °C. A constant sample volume of 5.00 mL was held for each experiment. Densities were found by weighing 5.00 mL of each solution. Five efflux times were recorded for each sample and the averages of these times are reported along with solution density and relative viscosity to 10% D_2O/90% H_2O (see ESI†). The mixed Group V–Group VI POM solutions are not corrected for viscosity due to the negligible variance at 5 mM.

2.5 PDF analysis of X-ray total scattering (XRTS)

The solutions of TMA{M_6} with added CsCl were prepared at 100 mM (with CsCl concentrations ranging from 100 to 1200 mM) in 200 mM TMAOH without D_2O. Raw X-ray scattering data were collected with a Rigaku Smartlab X-ray diffractometer with a Mo-Kα source (λ = 0.71073 Å). For these solution X-ray scattering measurements, an aliquot of the solution was injected in a Kapton 1.5 mm capillary, sealed and positioned in the goniometer. Transmission mode of the data collection was applied, where 2θ range of 3.0–118.6° was used. Therefore, the maximum available Q-value is 15.2 Å^{-1}. The data collection time was 0.2° min^{-1} using a 0.01 degree resolution. In order to eliminate the contribution of the solvent and the sample holder, Milli-Q water (Millipore, 18.2 MΩ at 25 °C) was also measured for background subtraction applying identical experimental parameters.

The solution scattering curves were transformed to the reduced structure functions, then they were Fourier transformed to obtain the reduced atomic pair distribution functions (PDF, denoted as $G(r)$ on the graph). For the mathematical transformations and background subtractions we used the PDFgetX3 software.[41] Simulated PDF data were obtained with the solX software[42] using the appropriate parameters.

2.6 Computational methods

Density functional theory (DFT) and time-dependent DFT (TD-DFT) calculations[43] were performed on single instances of $Cs_x[Ta_6O_{19}]^{(8-x)-}$ and $Cs_x[Nb_6O_{19}]^{(8-x)-}$ (x = 0, 1, 4, 8), using the software package Gaussian09.[44] Additional supplementary calculations were carried out on the series $M_8[Ta_6O_{19}]$ (M = Rb, K, Na, Li). In all cases, the chosen methodology is identical to the one previously employed by Deblonde *et al.* to compute the UV-Vis spectra of $[Ta_6O_{19}]^{8-}$ and $[Nb_6O_{19}]^{8-}$ in implicit water,[34] leading to results that were in excellent agreement with experiment.

This particular approach consists of two distinct steps, both involving spin-restricted calculations, but not relying on molecular symmetry. To begin with, all species are structurally optimized using the PBE0 functional:[45] at this stage, oxygen electrons are treated using the D95 basis set,[46] whereas those on remaining elements are modeled using various Stuttgart–Dresden effective core potential and basis sets. More specifically, tantalum electrons are treated with MWB60,[47] niobium with MWB28,[47] and cesium with MWB46.[48] With respect to the supplementary calculations on the $M_8[Ta_6O_{19}]$ series (M = Rb, K, Na, Li), rubidium electrons are treated with MWB28,[48] potassium with MWB10;[48] sodium with

SDF10;[49] and lithium with SDF2.[49] With hexatantalate salts in particular, convergence problems are occasionally encountered during default[50] solution of the self-consistent field equations; these are always solved by automatically invoking the alternative quadratic convergence procedure developed by Bacskay.[51] Structures resulting at this stage are also verified to be true minima by means of frequency calculations, aiming to confirm the absence of imaginary vibrational modes.

In the second and final step, the UV-Vis spectrum of each optimized structure of {M_6}; Cs{M_6}; Cs$_4${M_6}; and Cs$_8${M_6} (M = Nb, Ta) is subsequently computed by means of a single-point TD-DFT calculation:[43] in this case, the PBE0 functional is retained, but electrons on all elements are treated with the def2-TZVP effective core potential and/or associated basis set.[52] In the case of the supplementary $M_8[Ta_6O_{19}]$ series (M = Rb, K, Na, Li), the level of theory is identical, but UV-Vis spectra are not derived, so only DFT calculations suffice. All orbital energies quoted and discussed in this work are actually those calculated during this second and final step.

Throughout both steps, water effects are implicitly included using the polarizable continuum model (PCM),[53] which is readily implemented in Gaussian09. Moreover, to rule out the existence of lower-energy solutions of computed wavefunctions, these are always tested for any spatial- or spin-instability.[54]

The Bonding Energy Decomposition analysis was performed using the ADF2012 program system.[55,56] The PBE0[45] DFT GGA functional including scalar relativistic ZORA[57,58] approach was used together with the Slater triple-ζ plus polarization basis sets (TZP) in all atoms, which included frozen cores up to 4p for Mo and 1s for O and C atoms. Solvent effects were introduced non-explicitly by means of the COSMO model.[59,60] The values of the atomic radii correspond to the van der Waals radii derived by Klamt.[59,60] For Cs, a value of 3.205 Å was used. A data set collection of input files and computational results is available in the ioChem-BD repository[61] and can be accessed online.[62]

3 Results and discussion

3.1 NMR theory

NMR can be used to measure the relative magnitudes of ion-pairing between Cs^+ and various anions.[64,65] Because cesium's predominant isotope has a nuclear spin greater than $\frac{1}{2}$ (^{133}Cs, $I = \frac{7}{2}$),[66] it has a quadrupole moment.[67] Thus, cesium's nucleus can measurably interact with the electric field gradient arising from an asymmetric distribution of charge around it,[68] *i.e.*, from nearby charged anionic clusters. This interaction allows for an efficient relaxation mechanism, greatly outweighing weaker dipolar methods of relaxation to the point that they can be ignored,[69,70] including the Nuclear Overhauser Effect.[71] In light of this, the spin–lattice relaxation time parameter, T_1, and its reciprocal relaxation rate, R_{QR}, can be described entirely by quadrupole relaxation:

$$R_{QR} = \frac{1}{T_{1(QR)}} = \frac{3}{10}\pi^2 \frac{2I+3}{I^2(2I-1)}\left(1+\frac{\eta^2}{3}\right)\left(\frac{e^2Qq_z}{h}\right)^2 \tau_c \quad (1)$$

where η is an electric field gradient asymmetry parameter, q_z is the transverse electric field gradient, Q is the electric quadrupole moment of the nucleus, e is the electronic charge, τ_c is the molecular correlation time, and I is the nuclear spin.[72]

The molecular correlation time (τ_c) is expressed as:

$$\tau_c = \frac{4\pi\eta_0 r^3}{3kT} \qquad (2)$$

where η_0 is the viscosity of the solution, r is the effective hydrodynamic radius of Cs^+, k is the Boltzmann constant, and T is the temperature of the solution. The hydrodynamic radius of Cs^+ in water can be assumed to be independent of environment in the relatively dilute conditions in which we perform these experiments.[73,74] However, an assumption that viscosity varies negligibly between solutions of {Nb$_6$} and {Ta$_6$} cannot be made *a priori*. Further details regarding viscosity are discussed in the ESI.†

Ion pairing provides an efficient relaxation mechanism for the ^{133}Cs nucleus. It is thus possible to quantify ion-pairing and observe ion pairs, with larger values of R_{QR} (faster relaxation rates) indicating greater degrees of ion-pairing in solution. Each 1D ^{133}Cs spectrum contains only a single peak (Fig. S2, ESI†), indicating that the "free" and "bound" Cs^+ environments are in rapid exchange. Dipolar effects are further determined to be negligible due to rapid molecular reorientations occurring such that the extreme narrowing conditions apply.[75] The combined R_{QR} (upon adjusting for viscosity, R_{adj}) of the two Cs^+ environments in solution is the weighted average of their relaxation rates:

$$R_{adj} = \chi_b R_b + \chi_f R_f \qquad (3)$$

where χ_b and χ_f are the mole fractions of the bound and free environments and R_b and R_f are the quadrupolar relaxation rates of the bound and free environments, respectively. The value for R_f is the relaxation rate of ^{133}Cs at infinite dilution at 25 °C (0.086 s^{-1}).[63] Therefore, the relaxation rate for Cs^+ in an ion pair can be ascertained if the mole fractions of bound and free Cs^+ are known.

3.2 Quantification of Cs^+ ion-pairing as a function of charge density

^{133}Cs inversion-recovery NMR was performed on 5 mM solutions of a series of Cs-salts POMs with both Group V and Group VI metals ([TaW$_9$O$_{32}$]$^{5-}$, [NbW$_9$O$_{32}$]$^{5-}$, [Nb$_2$W$_4$O$_{19}$]$^{4-}$, [Nb$_4$W$_2$O$_{19}$]$^{6-}$, [Nb$_6$O$_{19}$]$^{8-}$, and [Ta$_6$O$_{19}$]$^{8-}$) to provide a systematic range of charge-densities. The cluster salts do not all have the same Cs : cluster ratio. Therefore this is a semiquantitative evaluation, since Cs-cations are likely to be in equilibrium between associated and free in solution. However, addition of excess Cs to the clusters of lower charge can induce precipitation. The POMs with more W(VI) centers have an overall lower charge and thus induce a smaller electric field gradient on nearby Cs^+ nuclei. Nonetheless, a Cs^+ in an ion pair with any of these anions will still have a significantly higher R_{QR} than the infinite dilution value due to the asymmetry of the charge distribution with respect to Cs^+. However, a single Cs^+ coordinated to multiple clusters in solution will exhibit an R_{QR} closer to the infinite dilution value due to the increased symmetry of the surrounding charge distribution (Fig. 1).

Cs associated with POMs of lower charge-density (more W) exhibit lower R_{QR} values than those of higher charge-density (more Nb or Ta), with tungsten-based POMs approaching the infinite dilution relaxation rate (Fig. 2). This is despite the fact that that there is higher Cs : cluster ratio for clusters of higher charge. As stated above, if all else is equal, a higher Cs : cluster ratio statistically means more Cs is free in solution leading to a slower relaxation rate, approaching that of Cs at infinite dilution. For the lower charge-density clusters, each Cs^+ is hydrated and separated from the anions or, at concentrations close to the solubility limit of the salt, presumably coordinated to multiple anions as observed in the structure of Cs$_4$Nb$_2$W$_4$O$_{19}$ (Fig. 1),[27] diminishing the quadrupolar relaxation rate. However, while there is a general trend of higher R_{QR} values (and thus greater average ion-pairing) with higher anionic charge density, the tantalum-containing POMs exhibit strictly faster quadrupolar relaxation rates than their niobium-containing counterparts of the same charge density in the case of both {M$_6$} (at the upper end) and {MW$_9$} (at the lower end). Thus, anionic charge-density is insufficient to fully explain the ion-pairing trends of Cs^+ in
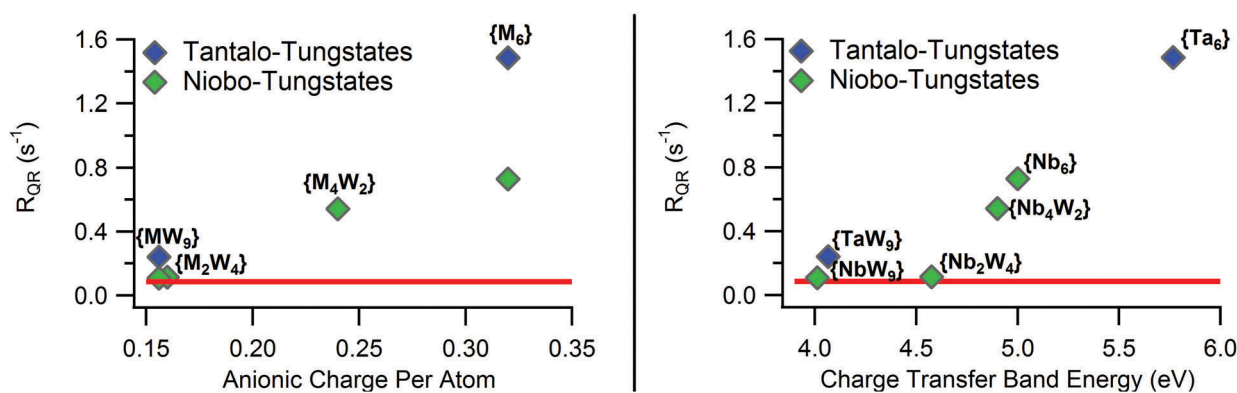

Fig. 2 ^{133}Cs quadrupolar relaxation rates of niobo- and tantalo-tungstates plotted with respect to (left) charge density of the anionic POM (total charge divided by the number of non-hydrogen atoms) and (right) the energy of the $n(O_{2p}) \rightarrow \pi^*(O_{2p}-M_{nd})$ charge transfer band measured by UV-Vis spectroscopy.[27,38] The red line indicates the literature value[63] of the ^{133}Cs R_{QR} rate at infinite dilution.

solution and more in-depth molecular orbital effects should be considered. Plotting R_{QR} instead against charge-transfer band energy (previously measured by UV-Vis spectroscopy) improves the monotonicity of the trend, although {TaW$_9$} remains an outlier (Fig. 2).

3.3 Comparing the Cs$^+$ ion-pairing of {Nb$_6$} and {Ta$_6$}

By observing solutions of Cs$_8$M$_6$O$_{19}$ (M = Nb, Ta; Cs{M$_6$}) at a range of concentrations with inversion-recovery ^{133}Cs NMR, we can fully ascertain the differences between {Nb$_6$} and {Ta$_6$} in how they interact with Cs$^+$ counter-cations. Previous thermochemical dissolution studies revealed that the enthalpy of dissolution for the Cs-salt of hexaniobate has a greater concentration dependence than for any other alkali salt, indicating different degrees of ion-pairing between dilute and more concentrated environments.[7] Inversion-recovery NMR experiments revealed a similar dependence of ion-pairing on concentration (Fig. 3). The quadrupolar relaxation rates of {Nb$_6$} and {Ta$_6$} exhibit an initial strong dependence on concentration, leveling out at higher concentrations. This trend indicates that the number of "bound" Cs$^+$ associated to each hexacoltanate anion increases with concentration, consistent with the previously observed decrease in dissolution enthalpy with increasing Cs{Nb$_6$} concentration. Notably, Cs$^+$ undergoes consistently faster relaxation when in solution with {Ta$_6$} than with {Nb$_6$}. This indicates that {Ta$_6$} undergoes a greater degree of ion-pairing with Cs$^+$ counter-cations than {Nb$_6$} at all concentrations. CsCl undergoes no ion-pairing and thus exhibits a constant R_{QR} independent of concentration.

A "snapshot" of the average degree of ion-pairing in solutions of Cs{M$_6$} can be obtained by dissolving solid CTAB (cetyltrimethylammonium bromide; C$_{16}$H$_{31}$(CH$_3$)$_3$NBr) into the cluster solutions at a range of concentrations. The resulting floc contains {M$_6$} anions with the ion-paired Cs$^+$ from the solution. CTA$^+$ balances the remaining charge and induces precipitation *via* interdigitiation of the hydrophobic surfactant tails. This is a departure from the typical behavior of most POM salts whose counter-cations are completely displaced by cationic surfactants.[76] In the case of Cs{M$_6$}, the Cs can never be fully displaced by this rapid precipitation process, giving an indication
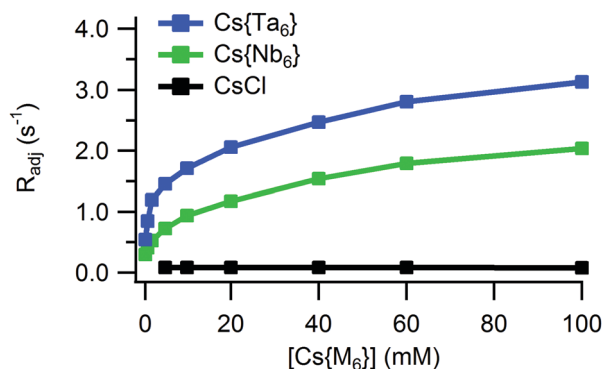
of how many Cs-cations are associated per cluster for any solution concentration. Therefore, we can directly compare the Cs$^+$/{M$_6$} ratio for {Nb$_6$} and {Ta$_6$} at the same concentration to corroborate our observation by NMR that there is more Cs$^+$ associated to hexatantalate than hexaniobate in water. Indeed, at each concentration tested, there are more Cs$^+$ per {Ta$_6$} than per {Nb$_6$} (Table 1). Moreover, the trend of increased ion association with increased solution concentration is also apparent in these studies. Excess CTAB was also added to a solution of only CsCl as a control, which yielded negligible (indistinguishable from the baseline) precipitated Cs (Fig. S10, ESI†).

Additionally, by considering the ratios of [Cs$^+$]/[{M$_6$}] (Cs$_{assoc}$) in tandem with R_{adj} for Cs$^+$ in each solution, along with the known R_f value (0.086 s^{-1}),[63] we can ascertain the value of R_b by rearranging eqn (3) (after multiplying both sides by 8 to reflect the 8 : 1 Cs$^+$: {M$_6$} ratio):

$$R_b = \frac{8R_{adj} - (8 - Cs_{assoc})R_f}{Cs_{assoc}} \qquad (4)$$

Because both {Nb$_6$} and {Ta$_6$} have an 8-charge, they induce very nearly identical electric field gradients on any Cs$^+$ ion in solution. Additionally, distances of Cs to the cluster's bridging oxygen atoms to which they are bound in the solid state are very nearly identical for Cs$_8$Nb$_6$O$_{19}$ and Cs$_8$Ta$_6$O$_{19}$ (≈ 3.1 Å).[23,77] The solution-state phase pair-distribution function data (PDF) described below for Cs{M$_6$} indicate the solid state structures are reliable models for solution ion-pairing, so the derived values for R_b in Table 1 are thus directly comparable. Upon averaging the values for R_b in Table 1, we estimate a value for the relaxation rate of a single Cs$^+$ in an ion pair with {M$_6$}:

$$R_b = 4.51 \pm 0.18 \text{ s}^{-1} \qquad (5)$$

From this value, we can calculate the relative populations of Cs$^+$ in an ion pair and "free" in solution for any solution of Cs$^+$ and {Nb$_6$} or {Ta$_6$} and thus the average number of Cs$^+$ ions in an ion pair per cluster in solutions of any concentration.

Cs$^+$ ion association can also be quantified by titrating CsCl into solutions of 20 mM (TMA)$_5$H$_3$Nb$_6$O$_{19}$ and (TMA)$_6$H$_2$Ta$_6$O$_{19}$. TMA$^+$ ions do not undergo any appreciable amount of ion-pairing with {M$_6$},[7,40] so any added Cs$^+$ may associate directly to the clusters without interference. However, the two compounds cannot be directly compared in neat water due to their differing protonation states and degrees of oligomerization in solution.

Fig. 3 Adjusted quadrupolar relaxation rates (R_{adj}) of Cs{Nb$_6$} and Cs{Ta$_6$} compared to CsCl, demonstrating the greater average Cs$^+$ ion pairing in {Ta$_6$}.

Table 1 Cs$^+$/{M$_6$} ratios in surfactant-precipitated samples along with associated R_b.[a] Cs$_{assoc}$ denotes the Cs/{M$_6$} ratio of the precipitate

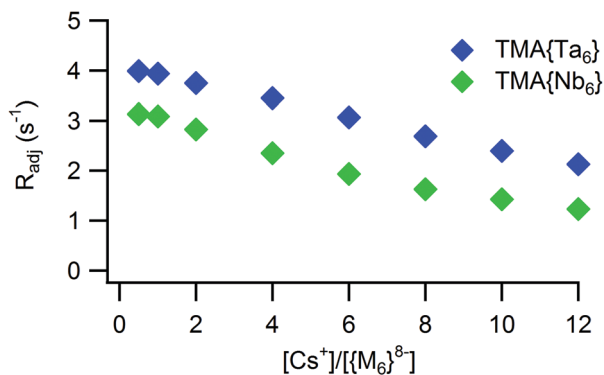| Starting solution	Cs$_{assoc}$	R_{adj} (NMR) (s^{-1})	R_b (s^{-1})
5 mM Cs{Nb$_6$}	1.14	0.719	4.52
10 mM Cs{Nb$_6$}	1.49	0.931	4.62
20 mM Cs{Nb$_6$}	2.11	1.169	4.19
5 mM Cs{Ta$_6$}	2.36	1.450	4.71
10 mM Cs{Ta$_6$}	2.97	1.712	4.46
20 mM Cs{Ta$_6$}	3.60	2.089	4.53

[a] R_b values are calculated from eqn (4).

Fig. 4 Quadrupolar relaxation rates of ^{133}Cs in a range of Cs$^+$/{M$_6$} ratios in 200 mM TMAOH, indicating the average degree of ion association upon the addition of CsCl.

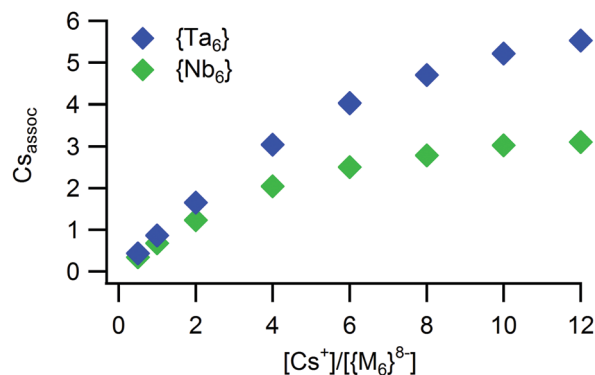Fig. 5 Number of associated Cs$^+$ per cluster in 20 mM solutions of TMA{M$_6$} (M = Nb, Ta) and 10–240 mM CsCl in 200 mM TMAOH. Values were obtained using eqn (6).

In light of this, they are instead observed in 200 mM TMAOH to ensure complete deprotonation and predominance of {M$_6$} monomers in solution,[40] while still keeping the viscosity of the solutions relatively low.

Cs$^+$ ion association as a function of Cs:{M$_6$} ratio (0.5–12) in 20 mM TMA{M$_6$} solutions was determined from ^{133}Cs R_{QR} measurements (Fig. 4). We again observe strictly greater Cs$^+$ ion association with {Ta$_6$} than with {Nb$_6$} at all Cs$^+$ concentrations. Although average Cs$^+$ ion association (*i.e.* the fraction of all Cs$^+$ in solution that is in an ion pair) decreases for solutions of both {Nb$_6$} and {Ta$_6$} with increasing Cs$^+$ as shown by R_{adj}, this does not indicate that there are fewer Cs$^+$ ions associated to any given cluster at higher [Cs$^+$]/[{M$_6$}] ratios. Instead, it suggests an equilibrium between free and associated Cs$^+$ and the equilibrium shifts more towards free Cs$^+$ as equivalents are added. By considering R_{adj} for each solution along with our derived value for R_b, we can arrive at an average Cs$_{assoc}$ in solution for any solution, again by rearranging eqn (3):

$$\text{Cs}_{assoc} = \frac{[\text{Cs}^+]}{[\{\text{M}_6\}]}\left(\frac{R_{adj} - R_f}{R_b - R_f}\right) \quad (6)$$

This yields a more intuitive picture of the degree of Cs$^+$ ion association that is presented in Fig. 5. Each curve also appears to approach a "carrying capacity" for associated Cs$^+$, with that of {Ta$_6$} being approximately double that of {Nb$_6$}. Thus, {Ta$_6$} undergoes greater degrees of ion-pairing than {Nb$_6$} with Cs$^+$ for any amount of initial free Cs$^+$ in solution.

3.4 The structure of the solution ion-pairing between Cs$^+$ and {M$_6$}

In order to define at atomistic model that accurately represents the binding of Cs$^+$ to the POMs, we need to know the solution 'structure'. Past small-angle X-ray scattering (SAXS) studies of the Cs-hexametalates have been executed in highly alkaline solutions with excess Cs$^+$,[9,26] and more recently in water alcohol mixtures.[78] Neither of these conditions are representative of the current experiments and, moreover, atomic-level ion pairs are not absolutely defined by SAXS. The prior studies also forced ion association by respectively a huge excess of Cs$^+$ and by

decreasing the solvent polarity. In the current system, we utilize conditions that simply ensure deprotonation of the clusters based on pH,[33] and variable stoichiometric amounts of Cs. Clearly evident in both the simulated PDF of {Ta$_6$} and the 100 mM TMA{Ta$_6$} without any added Cs is two strong peaks of *cis* Ta–Ta (3.4 Å) and *trans* Ta–Ta (4.8 Å) in the cluster (Fig. 6). There is also a weak peak around 2.0 Å that arises from the Ta–O bonds. Since the peak intensity is mostly determined by the scattering power of the elements, the peaks for M–M (M = metal) pairs are much more intense than those for M–O pairs. Although one can expect several peaks for the different metal–oxygen distances, only the first coordination sphere at ~2.0 Å is unambiguous and its intensity is significantly smaller than those at metal–metal distances. The peaks at greater distances have lower intensity in the experimental curves due to the inverse relationship between distance and peak intensity. Increasing the concentration of CsCl in the solutions results in a diminution of the water peak (~2.8 Å), which is exacerbated by the
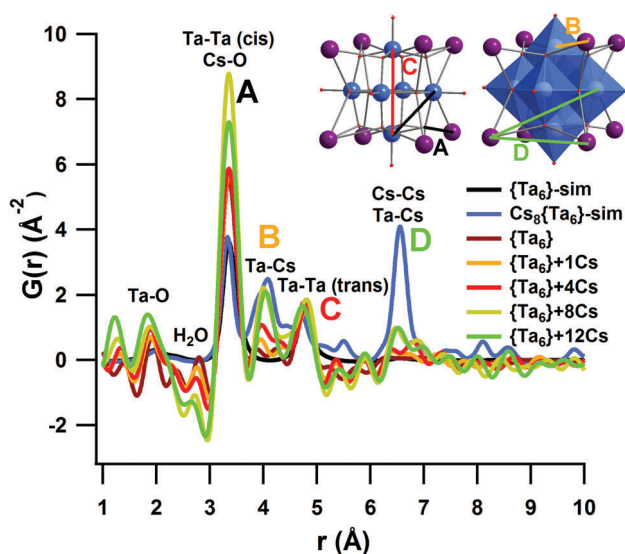

Fig. 6 PDF analysis of X-ray total scattering on solutions of 100 mM TMA{Ta$_6$} in 200 mM TMAOH with added CsCl (0 to 12 molar equivalents) – 'sim' indicates a simulated spectrum.

superposition with the shortest metal–metal distance (~ 3.4 Å). This phenomenon is common, since the hydration sphere of the free ions (Cs^+ and Cl^-) have contributions for this region and we can see the superposition of these different peaks in the short distance range.[79]

A distinct peak appears at 4.1 Å and becomes more intense with added CsCl. This distance is very close to the Ta–Cs distances seen in the solid state crystal structure of $Cs_8Ta_6O_{19} \cdot 14H_2O$,[39] confirming the similarity between the aqueous and solid state Cs^+ environments. Additionally, upon normalizing the peak heights at the *trans* Ta–Ta distance (4.8 Å), the Ta–Cs peak grows monotonically, reaching a maximum. This agrees with the determined 'carrying capacity' of Cs^+ from the above NMR experiments. The *cis* Ta–Ta distance at 3.4 Å, on the other hand, grows with added Cs^+. This pair distance overlaps with those of Cs–O and Cl–O pairs, according to prior X-ray scattering studies of CsCl and KCl solutions.[80,81] We can discount significant contribution from Cl–O due to both the disorder of water that is hydrogen-bonded to Cl^-,[79] as well as the relatively low electron density of this atom pair. On the other hand, the Cs–O pair produces significant scattering from Cs, and the number of Cs–O bonds formed is directly correlated with the number of Cs^+ in solution, regardless of whether they are bonded to water only or bonded directly to the cluster, with the rest of its coordination sphere completed with water molecules. Another peak arises at 6.6 Å with added Cs^+, attributable to either a *trans* Ta–Cs or Cs–Cs distance. The peak intensity monotonically increases with increasing Cs^+ concentration and does not exist in the absence of Cs^+.

The analogous $\{Nb_6\}$ solutions were also tested and exhibited very similar behavior to the $\{Ta_6\}$ solutions, with distinct Nb–Cs and Cs–Cs peaks growing monotonically with added Cs^+ at 4.1 Å and 6.7 Å (Fig. S3, ESI†). Thus the computational studies can be approached with confidence of correct solution phase structures. Moreover, these data provide a rare example of atomic-level evidence for ion-pairing in simple solutions that do not contain an excess of either the cation or anion.

3.5 Computational results

A contact ion pair, though impermanent and prone to rapid exchange with free ions in solution, involves some degree of covalent bonding.[82] The relative importance of pure ionic/electrostatic interactions *versus* covalent bonding can be ascertained within the framework of DFT, qualitatively from the analysis of the electronic structure and molecular orbitals (Kohn–Sham orbitals) composition and semi-quantitatively by applying the Bonding Energy Decomposition Analysis (EDA), for instance. A visualization of the evolution of the molecular orbital energy levels is included in Fig. 8, from single isolated $\{M_6\}$ ions and Cs^+, to 1-, 4- and 8-Cs^+ ion pairs, consistent with Fig. 7. The LUMO of $\{Ta_6\}$ is considerably higher in energy than that of $\{Nb_6\}$. The origin of the destabilized LUMOs for $\{Ta_6\}$ is the Ta_{5d} atomic orbitals mixing more poorly than Nb_{4d} with O_{2p} in the formation of $\pi^*(M_{nd}-O_{2p})$ frontier unoccupied molecular orbitals (Fig. S11, ESI†).

Upon the association of a single Cs^+ with $\{Nb_6\}$ and with $\{Ta_6\}$ (Fig. 7), the LUMOs of both are energetically stabilized (Fig. 8 and Table 2). The stabilization observed for the $Cs\{M_6\}$ LUMO in Fig. 8 is an indirect consequence of the interaction of the HOMO (primarily O^{2-} orbital character) with Cs^+. The contribution of Cs^+ to the HOMO can be seen clearly in Fig. 9, discussed further below. While some portion of this is attributable to the decrease in total charge from -8 to -7, stabilization of the $\{Ta_6\}$ LUMOs is nonetheless significantly greater than that of the $\{Nb_6\}$ molecular orbitals. When the number of associated Cs^+ ions is increased to four, we continue to see stabilization of both the HOMOs and LUMOs in both $\{Nb_6\}$ and $\{Ta_6\}$. However, we observe a greater total stabilization of the HOMO rather than the LUMO, resulting in a re-widening of the HOMO–LUMO gaps by roughly the same amount in both cases. Thus, when four Cs^+ ions are in a contact ion pair with a $\{M_6\}$ anion, the total stabilization of molecular orbital energies compared to when only one Cs^+ ion is associated is ascribable to the decrease in total charge of the assembly. In other words, the stabilization achieved upon forming a single $Cs\{M_6\}$ pair is largely diluted across the additional Cs^+ ions, rather than fully duplicated for each additional association. In the case where eight Cs^+ ions are associated (when the charge of the $\{M_6\}$ is fully neutralized), we again see stabilization of both the HOMOs and LUMOs, but such that the HOMO–LUMO gap increases (Tables S11 and S12, ESI†). Interestingly, the HOMO–LUMO gap of $Cs_8\{Nb_6\}$ is wider than that of $\{Nb_6\}$, but it is narrower in $Cs_8\{Ta_6\}$ than in $\{Ta_6\}$. This indicates that for any amount of

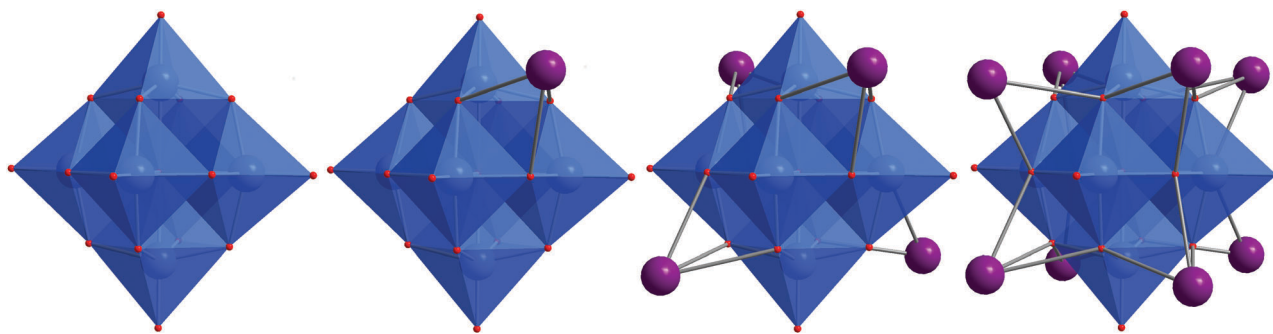**Fig. 7** Structures of (left to right) $\{M_6\}$; $Cs\{M_6\}$; $Cs_4\{M_6\}$; and $Cs_8\{M_6\}$ (M = Nb, Ta); optimized at the PBE0/Stuttgart–Dresden/D95 level (DFT). Key: small red spheres: O; large purple spheres: Cs^+; blue polyhedra: M. Gray lines are guides for the eye, and do not represent formal chemical bonds. All structures are also available on-line.
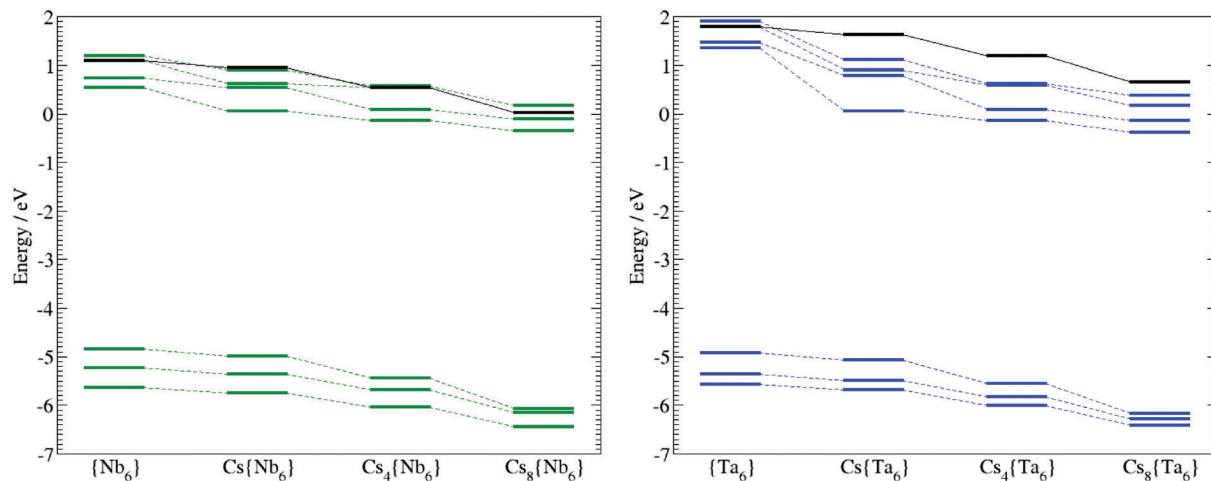
Fig. 8 Frontier molecular orbital energies of (left) {Nb$_6$} and (right) {Ta$_6$}, with 0, 1, 4, and 8 Cs$^+$ associated, as shown in Fig. 7. Black lines indicate the $\pi*(O_{2p}-M_{nd})$ frontier unoccupied molecular orbital.

Table 2 Bond energy decomposition terms for the interaction of a single Cs$^+$ ion with {Nb$_6$} and {Ta$_6$} and solvation energies. 'Non-relativistic' refers to results obtained by cancelling relativistic scalar ZORA effects. All energy values are in kcal mol^{-1}

	{Nb$_6$}		{Ta$_6$}		Cs$^+$	
	ZORA	Non-relativistic	ZORA	Non-relativistic	ZORA	Non-relativistic
Solvation energy	−2184.6	−2186.7	−2187.3	−2188.3	−50.4	−50.4

	Cs–{Nb$_6$}		Cs–{Ta$_6$}	
	ZORA	Non-relativistic	ZORA	Non-relativistic
Pauli repulsion	65.1	69.3	56.8	65.8
Electrostatic interaction	−547.4	−551.5	−546.4	−548.4
Orbital interactions (OI)	−19.2	−24.0	−28.8	−21.4
Bonding energy (BE)	−501.5	−506.3	−518.4	−504.1
%OI/BE	3.8	4.7	5.6	4.3
Solvation energy	−1719.4	−1720.7	−1715.1	−1724.3
Δ (solvation)	515.6	516.4	522.6	514.4
Total interaction energy	14.1	10.1	4.2	10.3

associated Cs$^+$, the LUMOs have still undergone more total stabilization than the HOMOs in {Ta$_6$}, whereas this is not the case for {Nb$_6$}. Electrostatic effects alone cannot explain this result.

The interaction between Cs$^+$ and both anions was analyzed in terms of the bond energy decomposition scheme.[83–85] Within this framework, the interaction energy is decomposed into three terms: two accounting for the interaction of the two unperturbed electronic densities (the Pauli repulsion and the electrostatic interaction) and a third term that accounts for the energy released because of the electronic relaxation, which is usually called "orbital interactions". This scheme is applied in the gas phase. Melgar *et al.* recently demonstrated that in order to apply this method to charged fragments in solution, the balance of solvation energies of all the species needs to be taken into account.[86] Following this protocol, the analysis was also carried out with and without including relativistic effects. As expected, the values in Table 2 show that the electrostatic

term is by far the most important and contributes equally in both cases. This term is slightly larger for {Nb$_6$}, as is the Pauli repulsion term. Both terms account for the slightly higher negative charge of the oxygen atoms in {Nb$_6$}. Significantly, the orbital interaction term clearly favors {Ta$_6$} over {Nb$_6$}. Whereas Pauli and electrostatic terms hardly change upon cancellation of relativistic effects, the difference in the orbital interaction term between {Ta$_6$} and {Nb$_6$} almost vanishes. The percentage of the orbital interaction with respect the Bonding Energy does not exceed 6% in {Ta$_6$} and 4% in {Nb$_6$}. Both values decrease and equalize when relativistic effects are cancelled out. It is important to notice that the total interaction energy values are slightly positive. This is due to the inaccuracy in computing absolute solvation energies. For instance, for Cs$^+$ we computed −50.4 kcal mol^{-1} while the experimental value is −47.5 kcal mol^{-1}.[87] The subtle balance between the Δ (solvation) term and bonding energy term finally generates a total interaction energy value of 4.2 kcal mol^{-1} for {Ta$_6$} – a reasonably

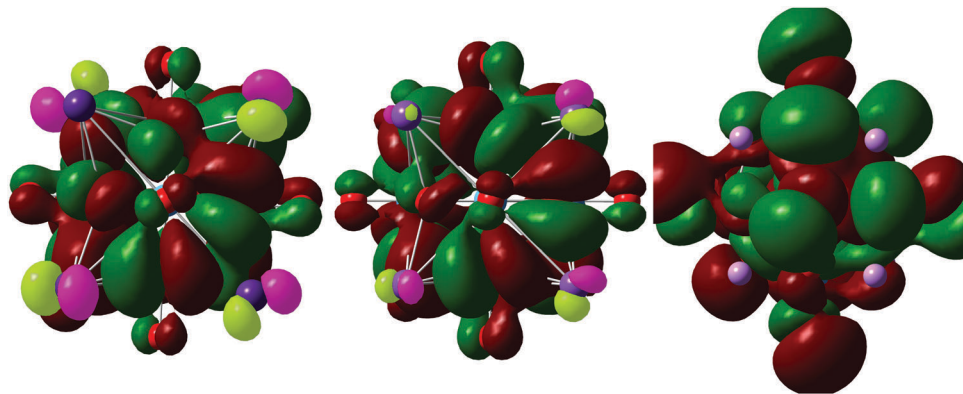**Fig. 9** Representation of the HOMO of (left) $Cs_8[Ta_6O_{19}]$; (center) $K_8[Ta_6O_{19}]$; and (right) $Li_8[Ta_6O_{19}]$; all with isosurface 0.005. The decreasing degree of admixture of alkali metal orbitals (seen in the sizes of the lobes on the alkali metals – highlighted in magenta and light green) is evident when going from left to right.

small number. Thus, relativistic effects clearly make the difference between $\{Ta_6\}$ and $\{Nb_6\}$.

Further, to obtain another perspective on the nature of Cs^+ bonding to $\{Ta_6\}$, we ran supplemental calculations[62] on the series $M_8[Ta_6O_{19}]$, where M = Rb, K, Na, Li (in this case without deriving UV-Vis spectra). Analysis of atomic orbital contributions, as well as energy plots of frontier orbitals for this series, are reported as ESI.† As expected, results from these additional calculations also point to a markedly covalent character in $Cs_8[Ta_6O_{19}]$, which gradually decreases from Cs to Li. For example, Fig. 9 depicts the HOMO of $Cs_8[Ta_6O_{19}]$, $K_8[Ta_6O_{19}]$, and $Li_8[Ta_6O_{19}]$, all with isosurface 0.005. Participation of Cs^+ orbitals is evident in the first case, much less pronounced in K^+ orbitals of $K_8[Ta_6O_{19}]$ and completely absent in the case of $Li_8[Ta_6O_{19}]$, where the interaction of Li^+ with $\{Ta_6\}$ is purely electrostatic in nature.

4 Conclusion

Through a combination of experimental and computational methods, we have arrived at a more thorough understanding of the nature of Cs^+ ion-pairing with polyoxometalates in water. Here we considered effects beyond relatively simple Coulombic models that cannot explain observed differences when charge-density is identical, as in the case of $\{Nb_6\}$ and $\{Ta_6\}$. The partial covalent nature of the $Cs\{Ta_6\}$ contact ion-pair, as shown by the extent of the mixing of the Cs^+ and the $\{M_6\}$ orbitals, was demonstrated by the higher value of orbital interaction energy in $Cs\{Ta_6\}$ than in $Cs\{Nb_6\}$. We owe this difference to relativistic effects, which was clearly shown by bond energy decomposition.

While scientists accept that in the solid state, bonds are rarely purely ionic or covalent, this is less widely accepted when describing aqueous solutions where all interactions are presumed to be ionic in nature. However, by computational studies and unexplained differences in ion-pairing experiments of Cs^+ with $\{Nb_6\}$ and $\{Ta_6\}$, we have arrived at a conviction that covalency in ion-interactions in water are relevant. Finally we return to the issue of solubility and understanding how the $Cs–\{M_6\}$ salts can be extremely soluble with maximum ion-pairing, contrary to well-known trends. The PDF reveals a remarkably stable

ion-interaction, in that it is rigid enough to produce a strong correlation peak between the Nb/Ta of the cluster and the associated Cs^+. Moreover, based on the solid state model, the Cs^+ forms three bonds to the cluster face, probably also contributing to the stability of the solution-phase interaction. We have surmised that the interaction is so strong between the cluster and Cs^+ that the Cs^+ does not bridge to other clusters, thereby hindering precipitation. Through ongoing experiments and calculations, we hope to quantify the critical feature of polyatomic anions (*i.e.*, charge density, size, type of ion-pairing) that drives the turning point from anomalous solubility behavior seen in the current system of study to normal solubility behavior. Through these investigations, we will ultimately ascertain a more general and complete set of rules by which the solubility of any given ion pair can be predicted based on the nature of both coulombic and covalent interactions in water.

Acknowledgements

References

1 J. D. Meyer and M. C. Manning, *Pharm. Res.*, 1998, **15**, 188–193.
2 M. Petrovi, S. Gonzalez and D. Barceló, *TrAC, Trends Anal. Chem.*, 2003, **22**, 685–696.

3   J.-F. Brière, S. Oudeyer, V. Dalla and V. Levacher, *Chem. Soc. Rev.*, 2012, **41**, 1696–1707.

4   M. M. Riès-Kautt and A. F. Ducruix, *J. Cryst. Growth*, 1991, **110**, 20–25.

5   M. Blesa, A. Weisz, P. Morando, J. Salfity, G. Magaz and A. Regazzoni, *Coord. Chem. Rev.*, 2000, **196**, 31–63.

6   J. Baumgartner, A. Dey, P. H. Bomans, C. Le Coadou, P. Fratzl, N. A. Sommerdijk and D. Faivre, *Nat. Mater.*, 2013, **12**, 310–314.

7   D. J. Sures, S. K. Sahu, P. I. Molina, A. Navrotsky and M. Nyman, *ChemistrySelect*, 2016, **1**, 1858–1862.

8   M. Nyman, *Dalton Trans.*, 2011, **40**, 8049–8058.

9   M. R. Antonio, M. Nyman and T. M. Anderson, *Angew. Chem.*, 2009, **121**, 6252–6256.

10 M. Nyman, F. Bonhomme, T. M. Alam, J. B. Parise and G. Vaughan, *Angew. Chem., Int. Ed.*, 2004, **43**, 2787–2792.

11 J. M. Pigga, J. A. Teprovich Jr, R. A. Flowers, M. R. Antonio and T. Liu, *Langmuir*, 2010, **26**, 9449–9456.

12 J. Zhang, B. Keita, L. Nadjo, I. M. Mbomekalle and T. Liu, *Langmuir*, 2008, **24**, 5277–5283.

13 M. K. Bera and M. R. Antonio, *J. Am. Chem. Soc.*, 2016, 7282–7288.

14 J. J. De Yoreo and P. G. Vekilov, *Rev. Mineral. Geochem.*, 2003, **54**, 57–93.

15 K. Nomiya, M. Kaneko, N. C. Kasuga, R. G. Finke and M. Pohl, *Inorg. Chem.*, 1994, **33**, 1469–1472.

16 J. D. Aiken and R. G. Finke, *J. Mol. Catal. A: Chem.*, 1999, **145**, 1–44.

17 S. J. Folkman, J. T. Kirner and R. G. Finke, *Inorg. Chem.*, 2016, 5343–5355.

18 R. E. Schreiber, L. Houben, S. G. Wolf, G. Leitus, Z.-L. Lang, J. J. Carbó, J. M. Poblet and R. Neumann, *Nat. Chem.*, 2016, 1–5.

19 C. L. Hill, *Chem. Rev.*, 1998, **98**, 1–2.

20 I. Correia, F. Avecilla, S. Marcão and J. C. Pessoa, *Inorg. Chim. Acta*, 2004, **357**, 4476–4487.

21 T. Oncsik, G. Trefalt, M. Borkovec and I. Szilagyi, *Langmuir*, 2015, **31**, 3799–3807.

22 T. M. Anderson, S. G. Thoma, F. Bonhomme, M. A. Rodriguez, H. Park, J. B. Parise, T. M. Alam, J. P. Larentzos and M. Nyman, *Cryst. Growth Des.*, 2007, **7**, 719–723.

23 M. Nyman, T. M. Alam, F. Bonhomme, M. A. Rodriguez, C. S. Frazer and M. E. Welk, *J. Cluster Sci.*, 2006, **17**, 197–219.

24 M. Nyman and P. C. Burns, *Chem. Soc. Rev.*, 2012, **41**, 7354–7367.

25 G. Dijkstra, W. H. Kruizinga and R. M. Kellogg, *J. Org. Chem.*, 1987, **52**, 4230–4234.

26 L. B. Fullmer, P. I. Molina, M. R. Antonio and M. Nyman, *Dalton Trans.*, 2014, **43**, 15295–15299.

27 D. J. Sures, P. I. Molina, P. Miró, L. N. Zakharov and M. Nyman, *New J. Chem.*, 2016, **40**, 928–936.

28 M. Chino, H. Nakayama, H. Nagai, H. Terada, G. Katata and H. Yamazawa, *J. Nucl. Sci. Technol.*, 2011, **48**, 1129–1134.

29 T. J. Yasunari, A. Stohl, R. S. Hayano, J. F. Burkhart, S. Eckhardt and T. Yasunari, *Proc. Natl. Acad. Sci. U. S. A.*, 2011, **108**, 19530–19534.

30 P. B. Du Bois, P. Laguionie, D. Boust, I. Korsakissok, D. Didier and B. Fiévet, *J. Environ. Radioact.*, 2012, **114**, 2–9.

31 D. McCabe, *Cesium, Potassium, and Sodium Tetraphenylborate Solubility in Salt Solution*, Westinghouse savannah river co., aiken, sc (united states) technical report, 1996.

32 R. C. Chapleski Jr, D. G. Musaev, C. L. Hill and D. Troya, *J. Phys. Chem. C*, 2016, **120**, 16822–16830.

33 E. Balogh, T. M. Anderson, J. R. Rustad, M. Nyman and W. H. Casey, *Inorg. Chem.*, 2007, **46**, 7032–7039.

34 G. J.-P. Deblonde, A. Moncomble, G. Cote, S. Bélair and A. Chagnes, *RSC Adv.*, 2015, **5**, 7619–7627.

35 G. J.-P. Deblonde, A. Chagnes, S. Bélair and G. Cote, *Hydrometallurgy*, 2015, **156**, 99–106.

36 G. J.-P. Deblonde, N. Delaunay, D. Lee, A. Chagnes, G. Cote and P. Gareil, *RSC Adv.*, 2015, **5**, 64119–64124.

37 M. Dabbabi and M. Boyer, *J. Inorg. Nucl. Chem.*, 1976, **38**, 1011–1014.

38 P. I. Molina, D. J. Sures, P. Miró, L. N. Zakharov and M. Nyman, *Dalton Trans.*, 2015, **44**, 15813–15822.

39 H. Hartl, F. Pickhard, F. Emmerling and C. Roehr, *ChemInform*, 2002, **33**, 2630–2638.

40 L. B. Fullmer, R. H. Mansergh, L. N. Zakharov, D. A. Keszler and M. Nyman, *Cryst. Growth Des.*, 2015, **15**, 3885–3892.

41 P. Juhás, T. Davis, C. L. Farrow and S. J. Billinge, *J. Appl. Crystallogr.*, 2013, **46**, 560–566.

42 X. Zuo, G. Cui, K. M. Merz, L. Zhang, F. D. Lewis and D. M. Tiede, *Proc. Natl. Acad. Sci. U. S. A.*, 2006, **103**, 3534–3539.

43 R. Bauernschmitt and R. Ahlrichs, *Chem. Phys. Lett.*, 1996, **256**, 454–464.

44 *Gaussian 09, Revision A.02*, Gaussian, Inc., Wallingford CT, 2009.

45 C. Adamo and V. Barone, *J. Chem. Phys.*, 1999, **110**, 6158–6170.

46 T. Dunning Jr and P. J. Hay, in *Modern Theoretical Chemistry*, ed. H. F. Schaefer III, 1977, vol. 3.

47 D. Andrae, U. Haeussermann, M. Dolg, H. Stoll and H. Preuss, *Theor. Chim. Acta*, 1990, **77**, 123–141.

48 T. Leininger, A. Nicklass, W. Küchle, H. Stoll, M. Dolg and A. Bergner, *Chem. Phys. Lett.*, 1996, **255**, 274–280.

49 P. Fuentealba, H. Preuss, H. Stoll and L. Von Szentpály, *Chem. Phys. Lett.*, 1982, **89**, 418–422.

50 K. N. Kudin, G. E. Scuseria and E. Cances, *J. Chem. Phys.*, 2002, **116**, 8255–8261.

51 G. B. Bacskay, *Chem. Phys.*, 1981, **61**, 385–404.

52 F. Weigend and R. Ahlrichs, *Phys. Chem. Chem. Phys.*, 2005, **7**, 3297–3305.

53 J. Tomasi, B. Mennucci and R. Cammi, *Chem. Rev.*, 2005, **105**, 2999–3094.

54 R. Bauernschmitt and R. Ahlrichs, *J. Chem. Phys.*, 1996, **104**, 9047–9052.

55 C. F. Guerra, J. Snijders, G. Te Velde and E. Baerends, *Theor. Chem. Acc.*, 1998, **99**, 391–403.

56 G. t. Te Velde, F. M. Bickelhaupt, E. J. Baerends, C. Fonseca Guerra, S. J. van Gisbergen, J. G. Snijders and T. Ziegler, *J. Comput. Chem.*, 2001, **22**, 931–967.

57 E. van Lenthe, E.-J. Baerends and J. G. Snijders, *J. Chem. Phys.*, 1994, **101**, 9783–9792.

58 E. van Lenthe, A. Ehlers and E.-J. Baerends, *J. Chem. Phys.*, 1999, **110**, 8943–8953.

59 A. Klamt and G. Schüürmann, *J. Chem. Soc., Perkin Trans. 2*, 1993, 799–805.

60 C. C. Pye and T. Ziegler, *Theor. Chem. Acc.*, 1999, **101**, 396–408.

61 M. Alvarez-Moreno, C. De Graaf, N. Lopez, F. Maseras, J. M. Poblet and C. Bo, *J. Chem. Inf. Model.*, 2014, **55**, 95–103.

62 *Input and output files for energy calculations*, https://doi.org/10.19061/iochem-bd-1-31.

63 D. D. Traficante, *Concepts Magn. Reson.*, 1997, **9**, 189.

64 A. I. Popov, *Pure Appl. Chem.*, 1979, **51**, 101–110.

65 W. J. DeWitte, R. C. Schoening and A. I. Popov, *Inorg. Nucl. Chem. Lett.*, 1976, **12**, 251–253.

66 V. W. Cohen, *Phys. Rev.*, 1934, **46**, 713.

67 N. Bloembergen and P. Sorokin, *Phys. Rev.*, 1958, **110**, 865.

68 H. A. Berman and T. R. Stengle, *J. Phys. Chem.*, 1975, **79**, 1001–1005.

69 J. A. Pople, W. G. Schneider and H. J. Bernstein, *High-resolution nuclear magnetic resonance*, McGraw-Hill, New York, NY, 1959.

70 J. E. Roberts and J. Schnitker, *J. Phys. Chem.*, 1993, **97**, 5410–5417.

71 F. W. Wehrli, *J. Magn. Reson.*, 1978, **30**, 193–209.

72 K. T. Gillen and J. H. Noggle, *J. Chem. Phys.*, 1970, **53**, 801–809.

73 C. Melendres and H. Hertz, *J. Chem. Phys.*, 1974, **61**, 4156–4162.

74 F. Wehrli, *J. Magn. Reson.*, 1977, **25**, 575–580.

75 D. W. Urry, *Bull. Magn. Reson.*, 1987, **9**, 109–131.

76 M. Nyman, D. Ingersoll, S. Singh, F. Bonhomme, T. M. Alam, C. J. Brinker and M. A. Rodriguez, *Chem. Mater.*, 2005, **17**, 2885–2895.

77 H. Hartl, F. Pickhard, F. Emmerling and C. Röhr, *Z. Anorg. Allg. Chem.*, 2001, **627**, 2630–2638.

78 L. Fullmer and M. Nyman, *J. Cluster Sci.*, 2017, **28**, 813–823.

79 V. Mile, L. Pusztai, H. Dominguez and O. Pizio, *J. Phys. Chem. B*, 2009, **113**, 10760–10769.

80 F. Li, J. Yuan, D. Li, S. Li and Z. Han, *J. Mol. Struct.*, 2015, **1081**, 38–43.

81 H. Ohtaki and N. Fukushima, *J. Solution Chem.*, 1992, **21**, 23–38.

82 K. Fajans and G. Joos, *Z. Phys.*, 1924, **23**, 1–46.

83 K. Kitaura and K. Morokuma, *Int. J. Quantum Chem.*, 1976, **10**, 325–340.

84 T. Ziegler and A. Rauk, *Inorg. Chem.*, 1979, **18**, 1755–1759.

85 F. M. Bickelhaupt and E. J. Baerends, *Rev. Comput. Chem.*, 2007, **15**, 1–86.

86 D. Melgar, N. A. Bandeira, J. B. Avalos and C. Bo, *Phys. Chem. Chem. Phys.*, 2017, **19**, 5343–5350.

87 K. P. Jensen and W. L. Jorgensen, *J. Chem. Theory Comput.*, 2006, **2**, 1499–1509.